CrossMark

TECHNICAL ARTICLE

Crystalline microstructure of boehmites studied by multi-peak analysis of powder X-ray diffraction patterns

Pablo Pardo,[1] Marek Andrzej Kojdecki,[2,a)] José Miguel Calatayud,[1] José María Amigó,[3] and Javier Alarcón[1]
[1]*Department of Inorganic Chemistry, University of Valencia, Valencia, Spain*
[2]*Institute of Mathematics and Cryptology, Military University of Technology, Warsaw, Poland*
[3]*Department of Geology, University of Valencia, Valencia, Spain*

(Received 20 September 2016; accepted 11 May 2017)

Nanocrystalline boehmite (gamma-aluminium-oxyhydroxide) is a material of industrial importance, the functionality of which follows from its crystalline microstructure. A procedure for preparing boehmite nanoparticles, comprising the formation of a precipitate by the alkalization of an aqueous solution of aluminium nitrate and subsequent hydrothermal aging, was previously elaborated. The application of an additive (maltitol or tartaric acid) to control the sizes and shapes of crystallites in the produced polycrystalline powder of boehmite was developed. The aim of this work is a study of the effect of the hydrothermal treatment time on nanocrystalline characteristics of boehmite, both in absence and in presence of the additive. The obtained materials were investigated by using X-ray diffraction (XRD) as principal technique and additionally by scanning and transmission electron microscopy. The multi-peak analysis of powder XRD patterns was applied to determine the prevalent crystallite shape, volume-weighted crystallite size distribution, and second-order crystalline lattice strain distribution being principal quantitative characteristics of the crystalline microstructure. Based on these characteristics, three types of the microstructure correlated with the production procedures were observed and discussed in detail. The nanoparticles of boehmites were found to be monocrystalline grains with characteristic habits and sizes of order of ten nanometers weakly dependent on the hydrothermal treatment time. © *2017 International Centre for Diffraction Data.*
[doi:10.1017/S0885715617000641]

Key words: boehmite, crystalline microstructure, crystallite shape, crystallite size distribution, second-order crystalline lattice strain distribution, X-ray diffraction, transmission electron microscopy, scanning electron microscopy

I. INTRODUCTION

Aluminium oxyhydroxide occurs in two polymorphs: boehmite (γ-AlOOH) and diaspore, (α-AlOOH) (Digne *et al.*, 2002). Boehmite [orthorhombic, with approximately: $a = 3.694$, $b = 12.214$, $c = 2.868$ Å; with space group: *Amam*; (Brühne *et al.*, 2008; Pardo *et al.*, 2015)] has been extensively studied, mainly because its structure enables a topotactic transformation into γ-alumina (γ-Al_2O_3; Krokidis *et al.*, 2001) being an oxide of great industrial interest, widely used as sorbent or catalyst or catalyst support, among others, in cracking (Corma and Fornes, 1990), isomerisation (Sanchez-Valente *et al.*, 2004), and dehydrogenation reactions (Zhao *et al.*, 2014).

Boehmite presents a structure of $Al(O,OH)_6$ octahedral layers stacked in [010] direction, linked by hydrogen bonds. Within the layers, the oxygen and hydroxyl groups define cubic close packing with Al^{3+} ions in octahedral sites. The ideal cleavage of the stacked layers implies only the breakage of hydrogen bonds, leaving the (010) surface uncharged, since aluminium and oxygen sites are fully saturated. Lateral faces (101), (100), and (001), on the contrary, show surface charge because of the presence of active hydroxyl groups derived from the surface reconstruction and protonation mechanisms of relaxation of Al ions with coordination frustration (Raybaud *et al.*, 2001). These differences between surfaces make the microstructure of boehmite determining its physical-chemical properties (the microstructure is understood as the constitution of a polycrystalline material at supra-molecular level, including the shapes, sizes, aggregations and deformations of crystallites and crystalline grains). In the topotactic transformation, γ-Al_2O_3 keeps the microstructure of boehmite that affects critical catalytic features of the former, following from the sizes and distributions of pores, crystallites, and grains (Guzman-Castillo *et al.*, 2001). The microstructure of boehmite can be tuned in the nanoscale through the control of preparation parameters in bottom-up procedures, like the presence of additives (Cai *et al.*, 2010; Chiche *et al.*, 2011; Xia *et al.*, 2013) pH (Mathieu *et al.*, 2007; Chen *et al.*, 2008), temperature (Kaya *et al.*, 2002) or aging time (Pardo *et al.*, 2015). It allows the preparation of nanostructured alumina (Digne *et al.*, 2010; Shen *et al.*, 2012), recently applied in optics, biosensors and biomedicine (Chen *et al.*, 2015a, 2015b, 2015c). New uses of boehmite as vaccine adjuvant (Edelman, 1980, 2001) have been lately developed. Besides

a)Author to whom correspondence should be addressed. Electronic mail: m_kojdecki@poczta.onet.pl or Marek.Kojdecki@wat.edu.pl

https://doi.org/10.1017/S0885715617000641 Published online by Cambridge University Press

the use as γ-Al_2O_3 precursor, boehmite nanoparticles were applied in: the entrapment of proteins to enhance their thermal stability (Rutenberg *et al.*, 2013), the bone implants with improved osteoblast functions (Price *et al.*, 2003; Webster *et al.*, 2005), the encapsulation of bacteria to increase their viability in bio-sensors and bio-reactors (Amoura *et al.*, 2007), the adsorption (Auxilio *et al.*, 2008; Cai *et al.*, 2009; Zenobi *et al.*, 2010), and the selective recognition (Delgado-Pinar *et al.*, 2011; Wei *et al.*, 2011) of pollutants from the environment, the preparation of imaging agents in biomedicine (Delgado-Pinar *et al.*, 2007, 2011) and the preparation of new generation of LEDs (Bai *et al.*, 2014). Both these recent applications and the use as nanostructured alumina precursors strongly depend on the size and shape of the nanoparticles that through the relative proportion of exposed crystal faces determine such properties as reactivity (Guzman-Castillo *et al.*, 2001) or colloidal stability (Pardo *et al.*, 2014).

In any study of the microstructure of a polycrystalline material, X-ray diffraction (XRD) is a powerful tool that enables the determination of the shapes, sizes, and strains of the coherent-diffraction domains (i.e. crystallites). Advanced methods, based on multiple XRD line-profile analyses, feature the modelling of the morphology and size distribution of crystallites and provide much more information than the averaged crystallite size obtained by simplified single-line analysis methods proposed by Scherrer (1918) and Langford (1978). The application of the advanced methods is of special interest in the study of nanomaterials usually comprising single crystallites as constitutive particles (i.e. monocrystalline grains); one can take advantage of the high statistical significance of XRD in the determination of the sizes and shapes of such nanoparticles. The boehmite particles generally show angles between faces corresponding to those between crystallographic planes (Chiche *et al.*, 2011; Moreaud *et al.*, 2012), that agree with the expected crystal habits (Santos *et al.*, 2009) and support the hypothesis of monocrystallinity (Bokhimi *et al.*, 2002; Jolivet *et al.*, 2004; Chiche *et al.*, 2009) confirmed also by the observations of electron diffraction diagrams (Tettenhorst and Hofmann, 1980; Chen *et al.*, 2008). An exception to this happens when boehmite is prepared in acid media; under these conditions, boehmite particles show acicular shapes formed by the oriented aggregation of small platelets (Jolivet *et al.*, 2008). The application of the simplified XRD methods to studying boehmite microstructure is usual (Bokhimi *et al.*, 2001a, 2001b; Okada *et al.*, 2002; Nguefack *et al.*, 2003; Mathieu *et al.*, 2007), while the advanced methods of XRD line-profile analysis are rarely used. Up to the knowledge of the authors, only Chiche *et al.* (2008) made an approach using the Debye formula to simulate morphology-dependent diffraction patterns, which were compared with the experimental line profiles; Lock *et al.* (2010) have exploited harmonic functions to model the prevalent crystallite shape and mean size by neglecting both strains and distribution of sizes.

In a recent work devoted to the improvement of the dispersibility of boehmite nanoparticles (Pardo *et al.*, 2014), the evolution of the system in the course of the hydrothermal process, monitored initially through electron microscopy and simplified XRD analysis, evidenced the interest in a more detailed study of microstructure. With this aim an advanced XRD method for determining the microstructure, based on a realistic mathematical model of a polycrystal (Kojdecki *et al.*, 2007), has been applied to investigate the effect of the hydrothermal treatment time on the size and shape of nanoparticles in new sets of specimens produced both in absence and presence of an additive. The general mechanism of boehmite nanoparticle growth will be discussed with, considering the microstructural characteristics obtained by exploiting a method of multi-peak powder XRD pattern analysis. The modification of the mechanism induced by the additives will also be elucidated.

II. EXPERIMENTAL SECTION

A. Preparation procedure

The preparation of boehmite nanoparticles consisted of the formation of a precipitate by the alkalization of an aqueous solution of aluminium nitrate and its subsequent hydrothermal aging. This method, previously described in the literature (Jolivet *et al.*, 2004), was modified by performing the precipitation step at high temperature, i.e. 100 °C, that favoured the formation of boehmite among other aluminium hydroxide phases in other synthetic routes (Yoldas, 1973).

The procedure used in this work was described elsewhere (Pardo *et al.*, 2014) in detail. It started with heating an initial 0.1 M $Al(NO_3)_3 \cdot 9H_2O$ (Panreac) solution to 100 °C; 5 M NaOH was then added dropwise until pH raised from its initial value (ca. 2) to 10; a white precipitate was formed during the addition. After 2 h the suspension containing the precipitate was cooled to room temperature, then placed in PTFE lined stainless steel autoclaves and hydrothermally aged for 24, 72, 120, and 168 h at 200 °C. The resulting suspension was centrifuged and the isolated solid was washed three times with water and then finally dried overnight in a furnace at 100 °C. In the preparations with additive, a concentration of 0.01 M of either tartaric acid ($C_4H_6O_6$, Sigma-Aldrich) or maltitol ($C_{12}H_{24}O_{11}$, Sigma-Aldrich) was applied in the initial aqueous solution and the above-described procedure was performed. Boehmite specimens of this work were labelled with a character indicating that no additive (B0), tartaric acid (BT) or maltitol (BM) was used at the precipitation stage, followed by the corresponding hydrothermal treatment time, e.g. B024.

B. Materials characterisation

In this work the study of properties of boehmite nanoparticles focuses the evolution of microstructural characteristics in dependence on hydrothermal treatment time, to complement a previous study principally related to the compositions of initial aqueous suspensions (Pardo *et al.*, 2014).

1. Electronic microscopy observations

The size and shape of the final nanoparticles were observed by transmission electron microscopy (TEM) in a Jeol 1010 (Tokio, Japan) working at 100 kV. Samples were prepared by dispersing as-produced powder in water and setting drops of the suspension on a copper grid that had previously been coated with a holey thin carbon film. Field emission scanning electron microscopy (SEM) observations were performed in a Hitachi 4800 facility (Hitachi Ltd. Tokyo, Japan). The same suspensions as prepared for TEM observations were dropped on the surface of an aluminium

https://doi.org/10.1017/S0885715617000641 Published online by Cambridge University Press

holder. Before the examination specimens were coated with Au-Pd in an ion beam coater.

2. XRD analysis of crystalline microstructure

The XRD investigation of powder samples were performed in a Bruker D-8 Advance diffractometer, using Cu$K\alpha$ radiation, with 1 and 3 mm divergence and antiscattering slits respectively, and a 3°2θ range Lynxeye linear detector. X-ray powder diffraction patterns with large peak intensities were recorded for wide range of diffraction angles (2θ) from 5° to 120°2θ with the step size of 0.02°2θ and the accumulated counting time of 2 s. A reference XRD pattern from lanthanum hexaboride (NIST standard reference material 660a) was recorded at similar conditions to determine the diffractometer instrumental function from which the standard line profiles corresponding to boehmite Bragg angles were simulated.

A quantitative analysis of the crystalline microstructure of boehmite specimens was performed by means of a mathematical model of a polycrystalline material that had been discussed in detail earlier (Kojdecki *et al.*, 2007, 2009). In this model a polycrystalline sample is interpreted as a statistical population of crystallites, which are assumed to be domains with perfect crystalline alignment of atoms inside, each of them scattering X-rays in a coherent way independently of one another, being separated by amorphous zones of small-angle or large-angle boundaries, and randomly oriented in space. Each crystallite may form a separate crystalline grain or be a mosaic block as a part of a grain. In approximation, crystallites are assumed to have the same simple shape, being a prevalent one in reality. Each crystallite is assumed to be constituted by the perfect lattice but of lattice parameters varying from each other; point defects inside crystallites and stacking faults are omitted. In this way the second-order strain (or incompatibility strain) is considered as homogeneous but in general anisotropic inside an individual crystallite. Consequently, the variation of lattice parameters of the crystallites is characterised by the second-order crystalline lattice strain distribution, which may be interpreted as a density of probability of finding a crystallite in which the interplanar distances differ from those in the reference structure according to an assumed relationship (the reference structure is determined by the parameters averaged over all crystallites). This distribution is assumed to be independent of crystallite size and of crystallographic direction; the isotropy may be interpreted as a statistical result of random orientations of thousands of crystallites interacting mechanically in grains and contributing to each XRD line profile. The sizes of the crystallites are characterised by the volume-weighted crystallite size distribution (CSD), which may be interpreted as a density of probability of finding a crystallite of an assumed shape and size, taken with a weight proportional to its volume, in an analysed sample. The size of a crystallite is any of its linear dimensions, while the shape is described by the ratios of its characteristic dimensions (like edge lengths of a prism); either the size distribution or the shape are treated as model parameters. To compare the features of different populations of crystallites (with different prevalent shapes), the standardised crystallite size equal to the cube root of the volume is introduced. In the computations crystallites are modelled as spheres, cylinders (of rotation axis in the [001] direction), or orthorhombic prisms (with edges parallel to axes [100], [010], and [001]).

III. RESULTS AND DISCUSSION

A. Electron microscopy

This work aims to enhance the previous studies of the growth mechanism of boehmite nanoparticles by considering the crystalline microstructure in detail. In a first approach, some preliminary considerations on the characteristics of the nanoparticles can be drawn from the electron microscopy observation of the specimens. Figure 1 shows the TEM images of the samples aged for the longest time: B0168, BM168, and BT168. Differences in the sizes of the particles can be easily noticed, evidencing restriction in growth induced by the additives, previously reported in a number of studies (Mathieu *et al.*, 2007; Chiche *et al.*, 2009, 2011; Dash *et al.*, 2010). In sample B0168 prepared with no additives prismatic particles with edges of lengths over 50 nm (some of them with rounded corners) were observed [Figure 1(a)]. The relatively large volume of some particles produced darker or blurry areas depending on their orientation with respect to the projection plane. Smaller, rectangular-prismatic particles were observed in samples prepared with additives, displaying sizes under 25 nm in sample BM168 and under 15 nm in BT168. The occurrence of edge-wise lying particles in samples BM168 and BT168 (thinner, darker forms in images in Figures 1(b) and 1(c)] revealed large aspect ratios, which confirmed that in samples BM and BT the particles were rectangular platelets with thicknesses significantly smaller than sizes in perpendicular directions. It is worth mentioning that boehmite particle shapes commonly found, described as diamond-shaped platelets (Chiche *et al.*, 2009), were not observed in samples BM168 and BT168; only in sample B0168 similar particles with round corners were visible. That particular morphology is mostly found at early stages

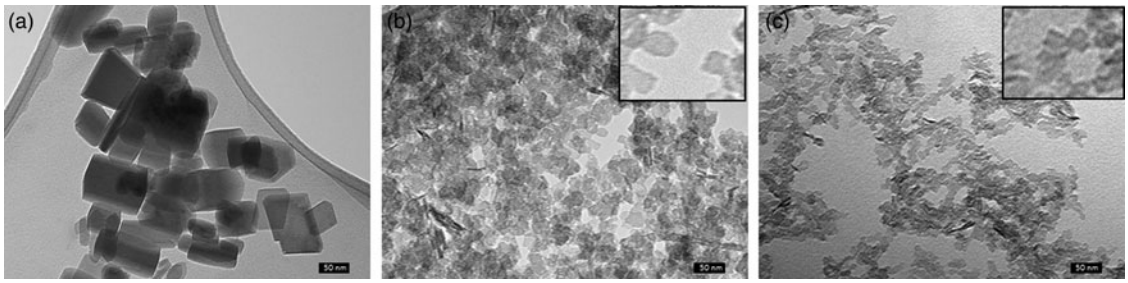


Figure 1. TEM images of the samples aged for the longest time, B0168 (a), BM168 (b), and BT168 (c). Particles of form of an orthorhombic prism (some of them with rounded corners) of edge lengths mostly around 50 nm (a) or 20 nm (b) or 10 nm (c), are clearly distinguishable.

https://doi.org/10.1017/S0885715617000641 Published online by Cambridge University Press

of boehmite crystallisation, observed mainly when boehmite is prepared in basic aqueous media with relatively low temperatures or for short hydrothermal treatment times (Chen *et al*., 2008; Jolivet *et al.*, 2008; He *et al.*, 2009; Chiche *et al*., 2011). Within the samples of this study, this set of conditions were fulfilled by B024; Figure 2 shows TEM images of the samples prepared without additive in the different aging stages tested. The image in Figure 2(a), corresponding to sample B024, the diamond-shaped platelets can be easily recognized. With increasing the aging time the particles grew preferentially along [010] crystallographic direction coincident with the thickness of the platelets, as was recently reported (Pardo *et al*., 2015). This kind of growth led to the formation of more equiaxial shapes and prismatic forms observed in samples B072, B0120, and B0168, at the expense of the platelets initially formed. This morphology is in good agreement with the crystalline habit predicted from surface and interfacial energy calculations (Raybaud *et al*., 2001). A parallel discussion on the morphological evolution of particles in samples BM and BT was not possible since the crystal development was strongly hindered in the presence of additives that prevented the observation of size or morphological differences with aging times. Another important feature of B0 samples was the polydispersity of crystalline grains. When boehmite nanoparticles grew freely, they showed a wide range of sizes, as can be observed in Figure 2, where the smallest and biggest particles for each treatment time have been encircled. This kind of distribution is compatible with processes involving a nucleation step followed by a growth based on dissolution-reprecipitation (Eberl *et al.*, 1990), previously reported for this system (Okada *et al.*, 2002). The presence of tartaric acid or maltitol in the preparation process resulted in size distribution much less dispersed as a consequence of severe growth restriction imposed by both additives.

The SEM observations were performed in order to observe the morphological evolution of B0 samples. Figure 3 compares the aspect of particles in sample B024 (a) with those in sample B0168 (b). The SEM images showed, clearer than TEM projections, that the evolution from the initial thin diamond-shaped platelets to the final thicker prisms was observed after 168 h of hydrothermal treatment, evidencing the anisotropic crystal growth.

Measurements of thicknesses (presumably in [010] direction) of edgewise-lying particles in TEM images for B0 samples were performed to characterise the particle growth. The number-weighted size distributions computed from the TEM images were recalculated to volume-weighted distributions, as they result from XRD analysis of the microstructure. The thicknesses collected in Table I can be compared with the mean crystallite sizes in direction [010] (B) in Table II. Table I clearly shows the increase of mean thickness and standard deviation of the size distribution of nanoparticles with hydrothermal treatment time; both these parameters agree pretty well with the similar ones computed from XRD diffraction patterns displayed in Table II. The poor statistics intrinsic to this methodology prevent quantitative interpretation of the grain sizes.

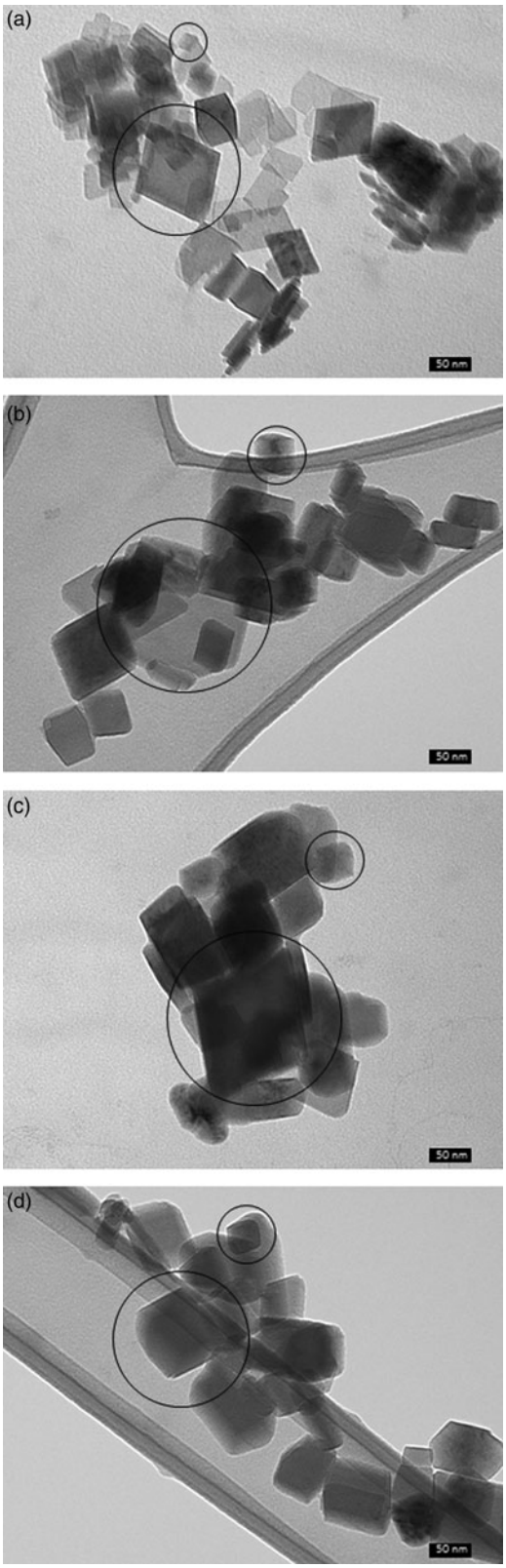


Figure 2. TEM images of boehmite samples prepared without additive with aging time 24 h (a), 72 h (b), 120 h (c), and 168 h (d). Both rectangular-prismatic and diamond-shaped particles are visible. The largest and the smallest particle images are encircled.

B. XRD analysis of microstructure

A set of non-overleaping peaks selected from the XRD pattern for each sample under study (Figure 4) was exploited as initial data for an inverse problem. After removing background modelled as low-order polynomial, pure XRD line profiles were computed with using instrumental line profiles and then microstructural characteristics were determined

https://doi.org/10.1017/S0885715617000641 Published online by Cambridge University Press

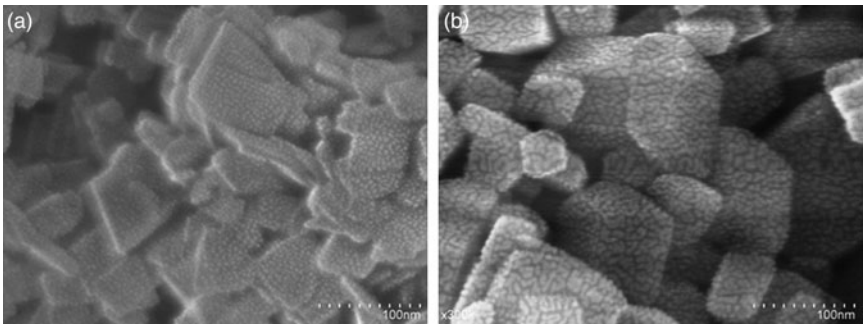


Figure 3. SEM images of samples B024 (a) and B0168 (b) evidencing the anisotropic crystal growth from platelet-like forms to equiaxial-prism-like forms.

through solving the inverse problem by regularisation method (since this inverse problem is ill-posed; e.g. Tikhonov *et al.*, 1995; Kojdecki, 2000). The mathematical model of a polycrystal was applied to modelling a corresponding XRD pattern with using microstructural characteristics as parameters and to formulating the inverse problem. Figure 5, Tables II and III collect the main results of application of the XRD analysis of crystalline microstructure. The results shown follow from the analysis of the diffraction line profiles corresponding to reflections 020, 120, 031, 131, 220, 151, and 080 (from B0 samples) or 020, 120, 031, 151, and 080 (from BM and BT samples). In Figure 5 basic microstructural characteristics are presented: volume-weighted standardised CSD and second-order crystalline lattice strain distributions (SD) for all samples. Averaged characteristics in Table III were calculated from these distributions. The best agreement between calculated and experimental XRD line profiles was achieved by considering the crystallites shaped as orthorhombic prisms with edges parallel to axes [100], [010], and [001]; for example seven measured and computed XRD peaks (after background subtraction) from sample B0168 are compared in Figure 6. Among those available in the applied methodology, this model was expected to provide the best results, especially after the observations of electronic microscopy images. For B0 and BM samples the modelling of the prevalent crystallite shape in form of rectangular parallelepiped (orthorhombic prism with edges in directions [100], [010], and [001]) as well as of cylinder of revolution (with axis in direction [001]) resulted in similar quality of approximation of experimental XRD peaks by simulated ones (Table II). In these specimens the most probable shape of crystallite was diamond-like prism with also contributing {110} faces. In corresponding TEM and SEM images similar prisms with rounded corners were observed.

The mean volume-weighted standardised crystallite sizes (T) for BM (7.5 ± 10.0 nm) and BT (4.8 ± 7.6 nm) samples were notably smaller than for B0 (30 ± 40 nm) samples, with BT samples showing the smallest sizes, in good agreement with the grain sizes observed in TEM images (Table II). The crystallite sizes increased with aging time in samples produced with no additive for 24 or 72 h of treatment; a longer-time hydrothermal treatment did not produce bigger crystallites. The presence of tartaric acid or maltitol restricted the growth of crystallites after the initial stages of aging although a slight increase of the mean crystallite sizes with aging time was observed (about 35% when the treatment time was prolonged from 24 to 168 h).

The mean volume-weighted sizes of prismatic crystallites in crystallographic direction [010] in samples B0 (size B in Tables II and III) were estimated quantitatively from size distributions following from XRD data and semi-quantitatively (because of small number of particles accounted for) from the particle thicknesses measured on TEM images (Table I). For each specimen both estimates agree well, especially when considering the coexistence of two fractions of crystallites and mean crystallite sizes for both fractions (Table III). These results suggest that the crystalline grains are mostly monocrystalline, i.e. each grain is a single crystallite.

The estimation of the shape factors revealed differences between the sets of samples. The aspect ratios of prism edge lengths B or C to A (shape factors P and Q, respectively) vary slightly with aging time (Table III); thus the mean values of both factors represent well different prevalent crystallite habit for each set of samples: $P \approx 1.0$, $Q \approx 0.7$ for B0, $P \approx 0.5$, $Q \approx 1.2$ for BM, $P \approx 0.8$, $Q \approx 1.5$ for BT (roughly similar to those observed by Lock *et al.*, 2010). In the boehmite nanoparticles produced without additive the shape factor P was always larger than in the particles produced in the presence of additive, indicating a larger development of the thickness of the initial platelets. The schematic representation of the shape and volume-weighted mean sizes of crystallites after 24 and 168 h of hydrothermal treatment, evidencing the different aspect ratios, is shown in Figure 7. The growth restrictions imposed by the additives induced also larger mean-absolute second-order strain (E) for BM and BT samples that remained almost independent of the aging time. On the contrary the mean strain for B0 samples, that after 24 h of hydrothermal treatment was about 50 or 30% of the corresponding values

TABLE I. Crystalline grain characteristics for B0 samples – mean prismatic particle thickness (presumably in [010] direction) with standard deviation, mode, minimal and maximal value computed from empirical volume-weighted size distribution determined immediately from TEM images; because of small number of particles analysed (n), intrinsic to this methodology, these characteristics are semi-quantitative.

Sample	Mean (nm)	Standard deviation (nm)	Mode (nm)	Minimum (nm)	Maximum (nm)	n
B024	25.2	8.4	10.0	4.5	39.8	31
B072	48.8	13.5	19.6	14.0	81.5	62
B0120	59.1	16.2	27.7	9.2	95.6	85
B0168	70.2	17.9	16.0	9.4	115.2	119

https://doi.org/10.1017/S0885715617000641 Published online by Cambridge University Press

TABLE II. Mean volume-weighted crystallite sizes and shapes computed from X-ray diffraction patterns by modelling crystallites as rectangular parallelepipeds [lengths of edges in directions [100] (*A*), [010] (*B*) and [001] (*C*) with length of base diagonal (*D*) and mean-standardised size (*T*)] or cylinders of revolution [diameter (*D*) in plane (001), height (*L*) and mean-standardised size (*T*)]. The errors of approximating set of XRD line profiles measured by simulated ones (RH) are smaller when assumed prismatic than assumed cylindrical crystallites, but for B0 and BT sets of samples they are close each other with similar mean sizes in direction [001] and in plane (001). It implies that the crystallites in these samples take forms in-between prism and cylinder e.g. like diamond-shape platelets with contributing (110) faces.

	Orthorhombic prism						Cylinder			
Sample	*A* (nm)	*B* (nm)	*D* (nm)	*C* (nm)	*T* (nm)	*RH*	*D* (nm)	*L* (nm)	*T* (nm)	*RH*
B024	35.3	33.1	48.4	22.9	29.9	0.108	39.7	23.6	30.8	0.104
B072	45.3	45.9	64.5	31.0	40.1	0.078	53.3	32.1	41.5	0.078
B0120	41.5	44.7	61.0	27.4	37.0	0.079	49.0	27.4	37.2	0.086
B0168	38.4	40.9	56.1	28.4	35.5	0.095	47.3	30.3	37.6	0.087
BM24	8.8	5.2	10.2	9.2	7.5	0.142	10.2	11.4	9.8	0.156
BM72	9.6	6.2	11.4	9.8	8.3	0.125	8.2	8.9	7.8	0.144
BM120	9.7	5.1	11.0	13.1	8.7	0.138	8.3	10.3	8.2	0.161
BM168	12.7	5.2	13.7	15.1	10.0	0.141	8.7	11.9	8.9	0.150
BT24	5.7	4.7	7.4	8.4	6.1	0.154	6.7	8.8	6.8	0.172
BT72	4.1	3.7	5.5	7.2	4.8	0.235	4.4	6.9	4.7	0.236
BT120	6.0	4.6	7.6	7.9	6.0	0.142	6.5	8.4	6.5	0.149
BT168	7.7	5.5	9.4	10.5	7.6	0.127	7.0	8.9	7.0	0.135

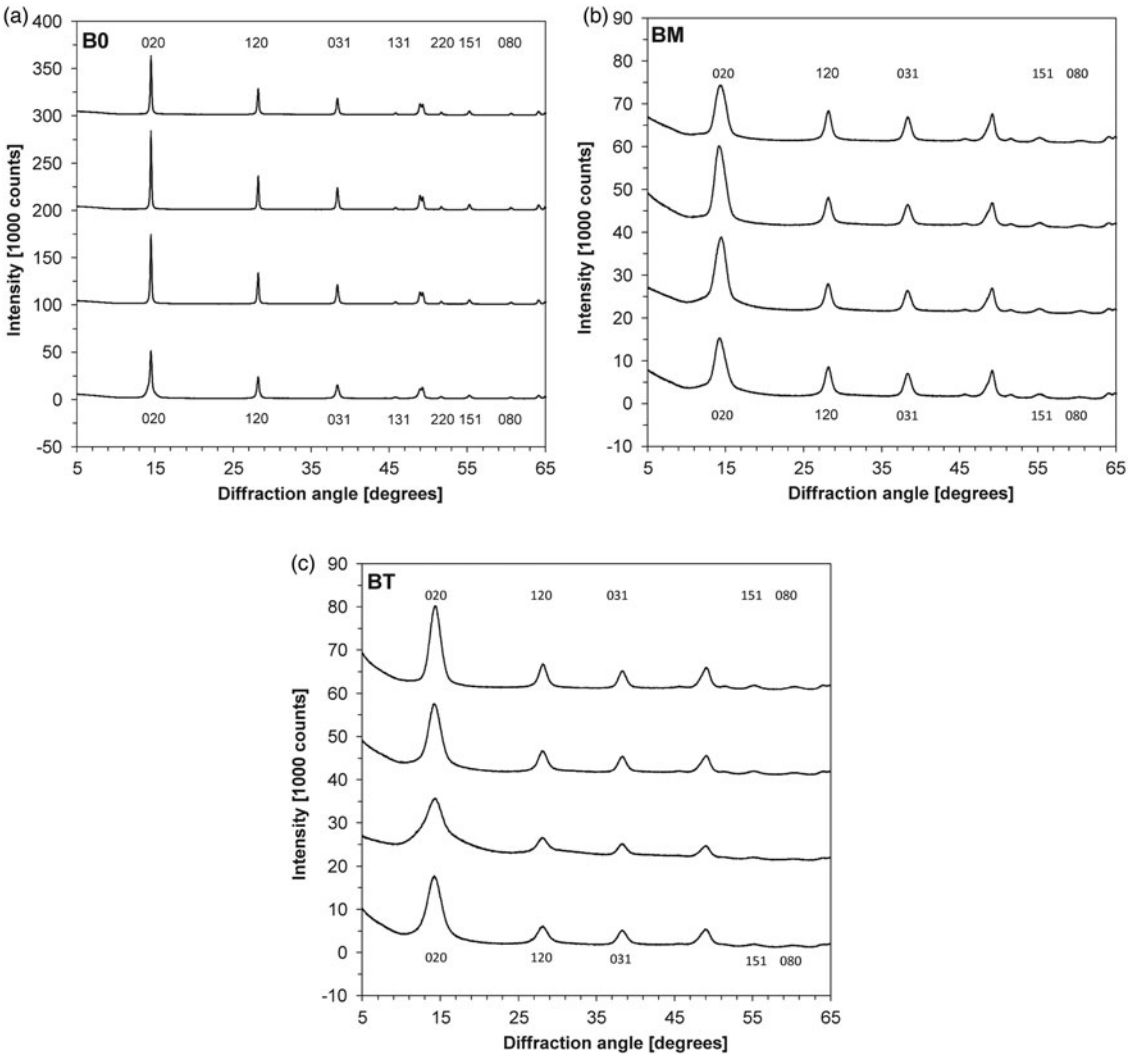


Figure 4. Fragments of XRD patterns with all peaks analysed for determining microstructural characteristics: (a) – from bottom to top B024, B072, B0120, B0168 shifted each other by a 100 000 counts; (b) – from bottom to top BM24, BM72, BM120, BM168 shifted each other by a 15 000 counts; (c) – from bottom to top BT24, BT72, BT120, BT168 shifted each other by a 15 000 counts; only the peaks used in computations are indexed.

https://doi.org/10.1017/S0885715617000641 Published online by Cambridge University Press

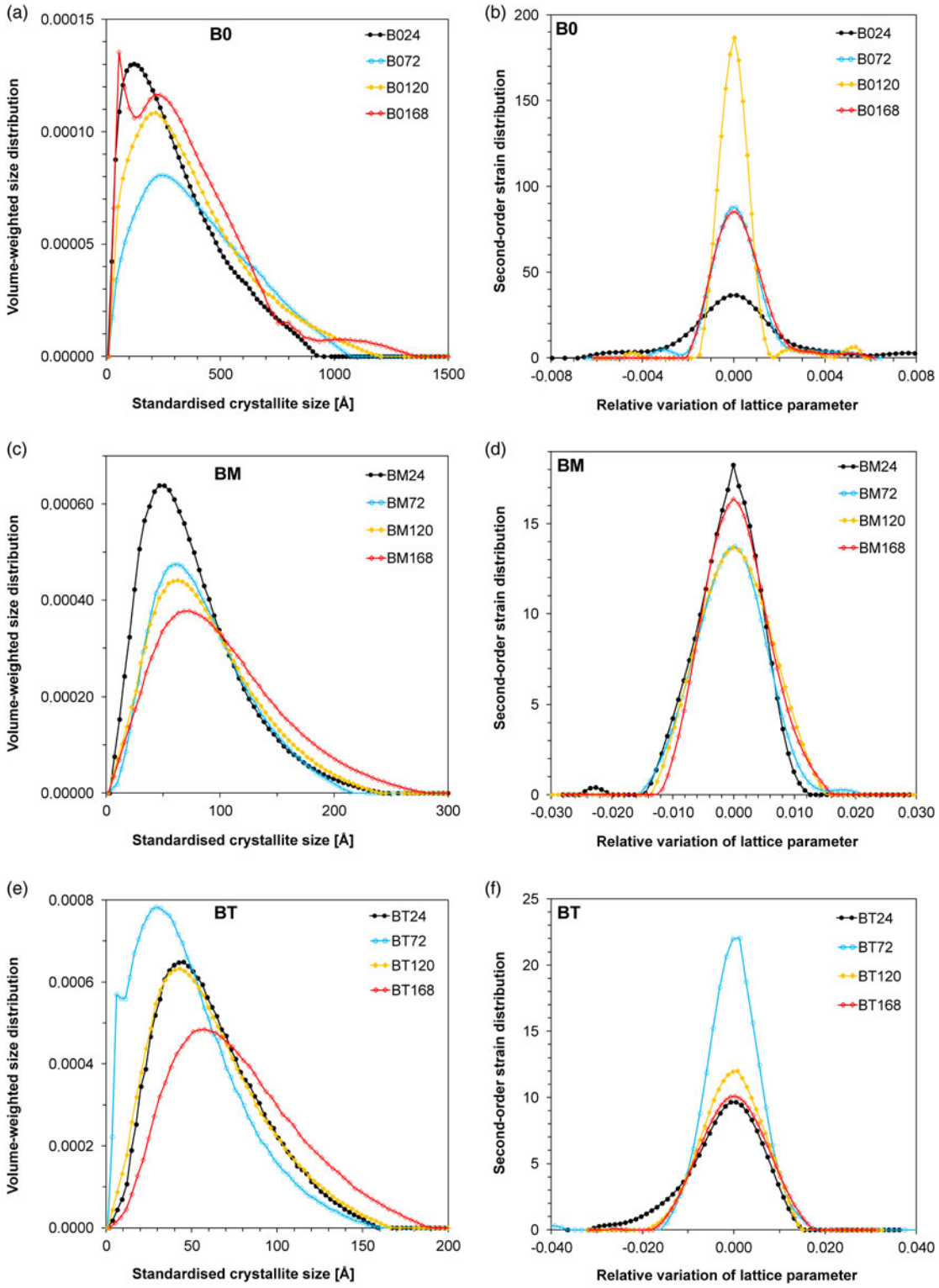


Figure 5. Volume-weighted standardised crystallite size distributions for samples B0 (a), BM (c), BT (e), and second-order crystalline lattice strain distributions for samples B0 (b), BM (d), BT (f).

for BM24 and BT24, decreased with aging time twice up to 72 h of treatment and remained almost independent of longer aging time. This observation is compatible with a recrystallisation process occurring after the initial stages of aging in the absence of additives. The second-order crystalline lattice strain distributions can be well approximated as Pearson's functions of type VII for boehmites processed for 24 or 72 h and of type II for those processed for 120 or 168 h (Figure 5, Table III).

C. Bimodality of CSD and growth mechanism

The calculated CSDs yield details of the crystalline microstructure featuring each set of specimens. The frequency

https://doi.org/10.1017/S0885715617000641 Published online by Cambridge University Press

TABLE III Average microstructural characteristics of boehmite computed from X-ray diffraction patterns by modelling crystallites as orthorhombic prisms and determined from volume-weighted crystallite size distributions and second-order crystalline lattice strain distributions: lengths of edges in directions [100] (*A*), [010] (B) and [001] (*C*) of a mean crystallite (for whole sample and for each fraction); prevalent aspect ratios ($P = B/A$, $Q = C/A$); mean-standardised crystallite size [$T = (ABC)^{1/3}$]; standard deviation for size distribution (*S*); mean-absolute second-order strain (*E*); standard deviation for strain distribution (*Z*); relative volume fraction content (*N*); quotient of fraction mean crystallite sizes; relative error of approximating selected set of XRD line profiles by profiles simulated for model polycrystal with microstructural characteristics determined from experiment (*RH*); relative error of approximating strain distribution (*RS*) by Pearson's II (*P*2) or VII (*P*7) function; relative error of approximating volume-weighted crystallite size distribution by bimodal (RB) or unimodal (RU) logarithmic-normal probability distribution.

Sample	*A* (nm)	*B* (nm)	*C* (nm)	*P* *N*	*Q* *T*2/*T*1	*T* (nm)	*S* (nm)	*S*/*T*	*E*	*Z*	*Z*/*E*	*RH* *RB*	*RS* *RU*
B024	35.3	33.1	22.9	0.94	0.65	29.9	19.6	0.66	0.001 79	0.002 52	1.41	0.108	0.063
F1	23.4	21.9	15.1	0.45		19.8	17.4	0.88					*P*7
F2	50.5	47.4	32.7	0.55	2.16	42.8	24.5	0.57				0.049	0.118
B072	45.3	45.9	31.0	1.01	0.68	40.1	22.9	0.57	0.000 93	0.001 31	1.40	0.078	0.073
F1	32.6	33.0	22.3	0.38		28.8	24.6	0.85					*P*7
F2	60.0	60.7	41.0	0.62	1.84	53.1	27.8	0.52				0.082	0.166
B0120	41.5	44.7	27.4	1.08	0.66	37.0	23.6	0.64	0.000 64	0.001 05	1.65	0.079	0.043
F1	26.0	28.0	17.2	0.35		23.2	20.9	0.90					*P*2
F2	53.9	58.1	35.6	0.65	2.07	48.1	28.6	0.59				0.036	0.129
B0168	38.4	40.9	28.4	1.06	0.74	35.5	24.4	0.69	0.000 89	0.001 20	1.35	0.095	0.082
F1	23.2	24.7	17.2	0.43		21.4	20.6	0.96					*P*7
F2	50.5	53.7	37.4	0.57	2.18	46.6	23.8	0.51				0.071	0.212
BM24	8.8	5.2	9.2	0.60	1.04	7.5	4.2	0.56	0.004 11	0.005 18	1.26	0.142	0.078
F1	7.6	4.5	7.9	0.45		6.5	5.0	0.76					*P*7
F2	10.6	6.3	11.0	0.55	1.39	9.0	4.8	0.53				0.030	0.076
BM72	9.6	6.2	9.8	0.64	1.02	8.3	4.0	0.48	0.004 46	0.005 55	1.24	0.125	0.041
F1	7.4	4.7	7.5	0.42		6.4	3.7	0.57					*P*7
F2	12.0	7.7	12.2	0.58	1.62	10.4	4.6	0.44				0.040	0.080
BM120	9.7	5.1	13.1	0.53	1.34	8.7	4.5	0.51	0.004 60	0.005 60	1.22	0.138	0.024
F1	8.3	4.4	11.2	0.40		7.4	5.4	0.73					*P*2
F2	11.7	6.2	15.7	0.60	1.40	10.4	5.0	0.48				0.047	0.104
BM168	12.7	5.2	15.1	0.41	1.18	10.0	5.2	0.53	0.004 16	0.005 15	1.24	0.141	0.049
F1	10.5	4.2	12.4	0.40		8.2	6.2	0.75					*P*2
F2	15.6	6.3	18.4	0.60	1.48	12.2	5.9	0.48				0.047	0.117
BT24	5.7	4.7	8.4	0.83	1.48	6.1	3.0	0.49	0.006 39	0.008 06	1.26	0.154	0.117
F1	4.4	3.7	6.6	0.44		4.8	2.8	0.58					*P*7
F2	7.1	5.9	10.6	0.56	1.61	7.7	3.4	0.44				0.045	0.081
BT72	4.1	3.7	7.2	0.92	1.76	4.8	3.0	0.62	0.004 79	0.006 98	1.46	0.235	0.038
F1	3.3	3.1	5.8	0.44		3.9	3.7	0.96					*P*7
F2	5.2	4.7	9.1	0.56	1.56	6.1	3.3	0.54				0.052	0.177
BT120	6.0	4.6	7.9	0.76	1.30	6.0	3.1	0.52	0.005 13	0.006 29	1.23	0.142	0.034
F1	5.2	4.0	6.8	0.44		5.2	3.7	0.71					*P*2
F2	7.4	5.6	9.6	0.56	1.42	7.3	3.5	0.48				0.047	0.097
BT168	7.7	5.5	10.5	0.71	1.37	7.6	3.6	0.47	0.005 48	0.006 71	1.22	0.127	0.011
F1	5.8	4.1	8.0	0.42		5.8	3.2	0.56					*P*2
F2	9.7	6.9	13.2	0.58	1.66	9.6	4.0	0.42				0.046	0.094

curves of CSDs for B0, BM, and BT samples are displayed in Figure 5. Each CSD can be well approximated by a bimodal logarithmic-normal function (much better than by an unimodal one); for example Figure 8 shows both approximations to the CDS for sample B024. A fraction of crystallites can be attributed to each component of a CDS. The main average characteristics of both fractions (corresponding to two components of CSD) and of whole sample are presented in Table III for all samples.

Some observations are worth mentioning: by considering the mean fraction crystallite sizes ($T1$ and $T2$) of both component of each CSD it can be noticed that the $T2/T1$ ratio was always larger in B0 samples ($T2/T1 \approx 2.1$) than in the others ($T2/T1 \approx 1.5$ in BM and $T2/T1 \approx 1.6$ in BT). The standard deviations of the CSD components for both fractions were roughly equal in each set of samples and thus the variation coefficient for the second fraction of crystallites was always smaller than for the first one. In BM and BT samples, on the other hand, the values of standard deviation of the CDSs were noticeably smaller than in B0 samples and approximately equal for both components with variation coefficient for the first fraction smaller than in B0 samples. These numbers feature evidently two different types of microstructure: $S1 \approx 20.9$, $S2 \approx 26.2$ *nm*, $S1/T1 \approx 0.90$, $S2/T2 \approx 0.55$ for B0 samples and common $S1 \approx 5.1$, $S2 \approx 5.1$ *nm*, $S1/T1 \approx 0.70$, $S2/T2 \approx 0.48$ for BM samples or $S1 \approx 3.4$, $S2 \approx 3.6$ *nm*, $S1/T1 \approx 0.70$, $S2/T2 \approx 0.47$ for BT samples (Table III). In all cases, the second fraction represented a slightly larger volumetric percentage ($N2 \approx 0.58$).

The existence of a range of crystallite sizes in the hydrothermally produced samples has been previously interpreted as an evidence of the occurrence of Ostwald ripening (Eberl *et al.*, 1990). After nucleation, surface free energy tends toward a minimum by the dissolution of small particles and

https://doi.org/10.1017/S0885715617000641 Published online by Cambridge University Press

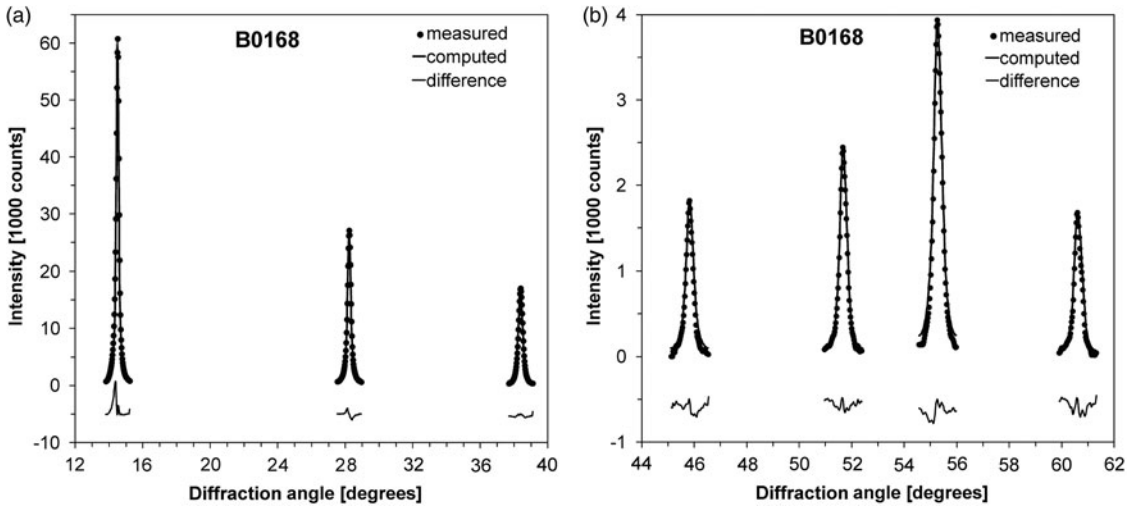


Figure 6. Experimental XRD line profiles (after background subtraction) and simulated XRD line profiles corresponding to crystalline microstructure characteristics revealed for sample B0168: (a) 12°–40° range of diffraction angles and (b) 44°–62° range of diffraction angles; the difference curve is shifted down by a 5000 counts.

the growth of large particles, as matter is transferred from the former to the latter. As the ripening proceeds in a closed system, the mean crystallite size increases, the level of supersaturation in the solution decreases, the particle size distribution widens, and the number of particles decreases. The thermodynamic basis of ripening is the size-dependence of the solubility of crystallites; when a crystal forms from a supersaturated solution there is a Gibbs free energy gain proportional to its volume, and a Gibbs free energy loss associated with the creation of its surface. Since the surface grows with size less than the volume, the energy gain balances the loss at a critical size (L_c) beyond which new nuclei are stable and can grow (Iggland and Mazzotti, 2012). A scheme of the processing of a substance is shown in Figure 9 with the solubility curve illustrating a solution concentration versus a critical size of a particle suspended in the solution. After the nucleation step produced in the additive-free precipitation and once the nuclei reached the critical size, the samples start growing under hydrothermal conditions with reducing the supersaturation of the solution. At that point, the critical size increases, and then Ostwald ripening becomes an important process, as a large amount of particles (corresponding to area under the curve at Figure 9) dissolve in favour of the particles of the over-critical size that continue growing. Since Ostwald ripening occurs at low supersaturation levels, driving forces are small, crystal growth and dissolution are very slow, and hence the process takes a long time (of days to months) (Iggland and Mazzotti, 2012).

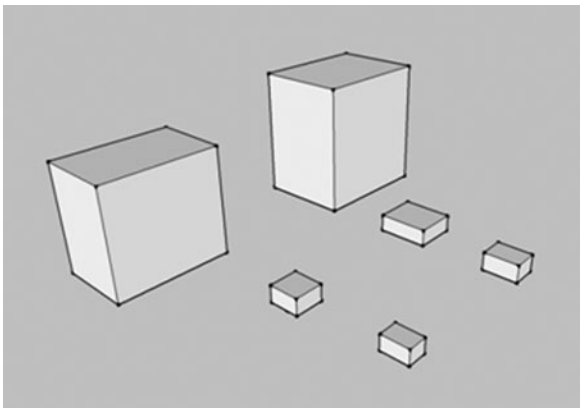


Figure 7. Schematic representation of prevalent shapes with mean volume-weighted sizes of crystallites after 24 (left) and 168 h (right) of hydrothermal treatment (the largest for B0 and the smallest for BT set of samples), evidencing the different aspect ratios.

The samples treated with additives presented some particularities. The formation of tartrate-aluminium complexes (Pardo *et al.*, 2014) modified the supersaturation in the tartaric acid. After the initial nucleation, the drop in supersaturation was faster than in the absence of additive. The ripening started with smaller particles, leading to narrower particle size distributions with less distant size modes, as observed in Figure 5. The interaction of maltitol with the lateral surfaces affected the dissolution-recrystallisation process. Once the crystallites displayed lateral active faces, maltitol molecules were adsorbed through the so-called nest effect (Chiche *et al.*, 2009), hindering further growing and recrystallisation processes. This kept the crystallite sizes small and, by slowing down the ripening, avoided the widening of the distributions.

The origins of the two fractions of crystallites were evident in two stages of crystallisation processes and different times of growth: the large crystallites of second fraction nucleated at precipitation stage and grew for longer time while the small crystallites of first fraction nucleated at hydrothermal treatment stage and grew for shorter time. The dispersions of sizes of crystallites around mean sizes in both fractions (i.e. standard deviations of both components of size distributions) remained equal or slightly different, as it was commented above.

IV. CONCLUSION

The method applied in this work of analysing selected line profiles of powder XRD pattern simultaneously enabled insight into details of crystalline microstructure of the investigated polycrystalline materials. The three principal quantitative characteristics of the microstructure: a prevalent crystallite shape, a volume-weighted CSD and a second-order

https://doi.org/10.1017/S0885715617000641 Published online by Cambridge University Press

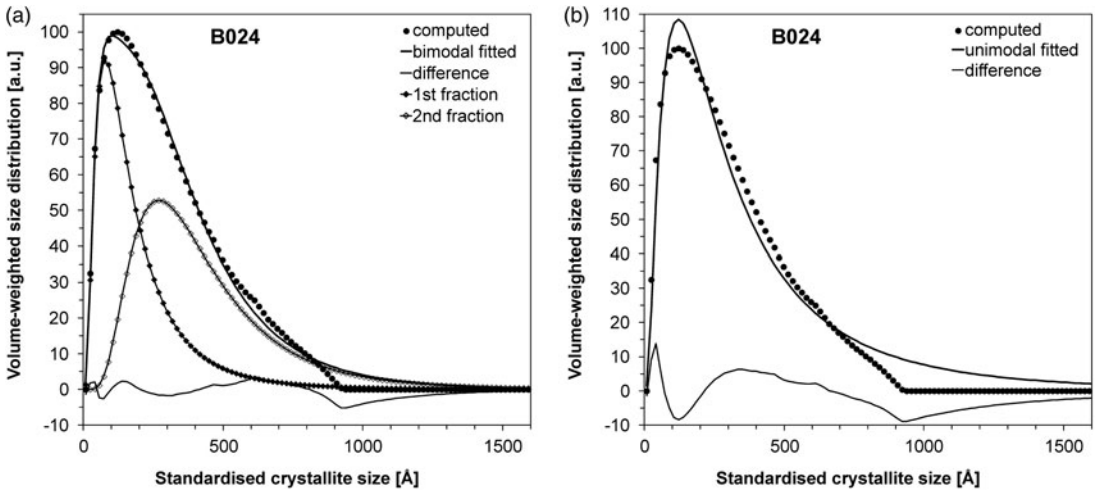


Figure 8. Bimodality of volume-weighted crystallite size distribution by example of sample B024. The distribution computed from experimental XRD data can be well approximated as (a) bimodal logarithmic-normal one (with relative error of 0.049 and fractions volume contents of 0.45 and 0.55), much better than as (b) unimodal logarithmic-normal one (with relative error of 0.118).

crystalline lattice strain distribution were determined reliably by solving an inverse problem with data extracted from XRD pattern for each specimen. These characteristics featured evidently three different types of the microstructure in the three sets of boehmite specimens as having been produced with no additive or with maltitol or with tartaric acid added to basic solution at the precipitation stage of production procedure.

The crystalline particles observed in SEM and TEM images were identified as being principally monocrystalline grains (i.e. single crystallites), as it followed from comparison of microstructural characteristics – quantitative from XRD and semi-quantitative from electron microscopy.

The two-stage procedure for preparing boehmite, comprising the precipitation from aqueous solution and the posterior hydrothermal treatment, produced two fractions of crystallites reflected in two logarithmic-normal components of CSD. The procedure was proved to be an effective method for producing boehmite nanoparticles with standardised sizes in the range between 5 and 40 nm. Slight changes of the crystalline microstructure with increasing hydrothermal treatment time were observed in the specimens produced with additives. In the specimens produced without an additive the hydrothermal treatment times of 72 h and larger all resulted in similar microstructures. Noticeable differences between the microstructures obtained after 24 and 72 h of hydrothermal treatment were observed only in the specimens produced with tartaric acid or without additive. The principal factor, which controlled the prevalent crystallite habit as well as the size and strain distributions, was an additive. The proper choice of the substance added at the precipitation stage is decisive for producing nanoparticles with required microstructural characteristics. Such procedures were studied and verified in this work successfully owing to application of the effective advanced method for determining microstructural parameters from powder XRD patterns.

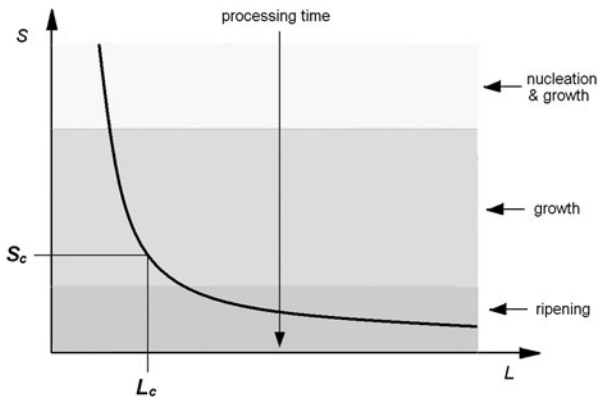


Figure 9. Schematic illustration of crystallite growth processes; the curve imitates the solution concentration (S) as a function of the critical size of a particle (L) suspended in the solution.

SUPPLEMENTARY MATERIAL

The supplementary material for this article can be found at https://doi.org/10.1017/S0885715617000641.

ACKNOWLEDGEMENTS

This work was financially supported by the Ministry of Science and Technology of Spain through project Consolider Ingenio 2010 CSD2010-00065 and Generalitat Valenciana through project Prometeo II/2015/002.

Amoura, M., Nassif, N., Roux, C., Livage, J., and Coradin, T. (**2007**). "Sol-gel encapsulation of cells is not limited to silica: long-term viability of bacteria in alumina matrices," Chem. Commun. **39**, 4015–4017.

Auxilio, A. R., Andrews, P. C., Junk, P. C., Spiccia, L., Neumann, D., Raverty, W., Vanderhoek, N., and Pringle, J. M. (**2008**). "Functionalised pseudo-boehmite nanoparticles as an excellent adsorbent material for anionic dyes," J. Mater. Chem. **18**, 2466–2474.

Bai, X., Caputo, G., Hao, Z. D., Freitas, V. T., Zhang, J. H., Longo, R. L., Malta, O. L., Ferreira, R. A. S., and Pinna, N. (**2014**). "Efficient and tuneable photoluminescent boehmite hybrid nanoplates lacking metal activator centres for single-phase white LEDs," Nat. Commun. **5**, 5702, 1–8.

Bokhimi, X., Toledo-Antonio, J. A., Guzman-Castillo, M. L., Mar-Mar, B., Hernandez-Beltran, F., and Navarrete, J. (**2001a**). "Dependence of boehmite thermal evolution on its atom bond lengths and crystallite size," J. Solid State Chem. **161**, 319–326.

https://doi.org/10.1017/S0885715617000641 Published online by Cambridge University Press

Bokhimi, X., Toledo-Antonio, J. A., Guzman-Castillo, M. L., and Hernandez-Beltran, F. (**2001b**). "Relationship between crystallite size and bond lengths in boehmite," J. Solid State Chem. **159**, 32–40.

Bokhimi, X., Sanchez-Valente, J., and Pedraza, F. (**2002**). "Crystallization of sol-gel boehmite via hydrothermal annealing," J. Solid State Chem. **166**, 182–190.

Brühne, S., Gottlieb, S., Assmus, W., Alig, E., and Schmidt, M. U. (**2008**). "Atomic structure analysis of nanocrystalline boehmite AlO(OH)," Cryst. Growth Des. **8**, 489–493.

Cai, W. Q., Yu, J. G., Cheng, B., Su, B. L., and Jaroniec, M. (**2009**). "Synthesis of boehmite hollow core/shell and hollow microspheres via sodium tartrate-mediated phase transformation and their enhanced adsorption performance in water treatment," J. Phys. Chem. C **113**, 14739–14746.

Cai, W. Q., Yu, J. G., Gu, S. H., and Jaroniec, M. (**2010**). "Facile hydrothermal synthesis of hierarchical boehmite: sulfate-mediated transformation from nanoflakes to hollow microspheres," Cryst. Growth Des. **10**, 3977–3982.

Chen, X. Y., Zhang, Z. H., Li, X. L., and Lee, S. W. (**2008**). "Controlled hydrothermal synthesis of colloidal boehmite (gamma-AlOOH) nanorods and nanoflakes and their conversion into gamma-Al_2O_3 nanocrystals," Solid State Commun. **145**, 368–373.

Chen, Y. T., Santos, A., Wang, Y., Kumeria, T., Li, J. S., Wang, C. H., and Losic, D. (**2015a**). "Biomimetic nanoporous anodic alumina distributed bragg reflectors in the form of films and microsized particles for sensing applications," ACS Appl. Mat. Interfaces **7**, 19816–19824.

Chen, Y. T., Santos, A., Wang, Y., Kumeria, T., Wang, C. H., Li, J. S., and Losic, D. (**2015b**). "Interferometric nanoporous anodic alumina photonic coatings for optical sensing," Nanoscale **7**, 7770–7779.

Chen, Y. T., Santos, A., Wang, Y., Kumeria, T., Ho, D. N., Li, J. S., Wang, C. H., and Losic, D. (**2015c**). "Rational design of photonic dust from nanoporous anodic alumina films: a versatile photonic nanotool for visual sensing," Sci. Rep. **5**.

Chiche, D., Digne, M., Revel, R., Chaneac, C., and Jolivet, J. P. (**2008**). "Accurate determination of oxide nanoparticle size and shape based on X-ray powder pattern simulation: application to boehmite AlOOH," J. Phys. Chem. C **112**, 8524–8533.

Chiche, D., Chizallet, C., Durupthy, O., Channeac, C., Revel, R., Raybaud, P., and Jolivet, J. P. (**2009**). "Growth of boehmite particles in the presence of xylitol: morphology oriented by the nest effect of hydrogen bonding," Phys. Chem. Chem. Phys. **11**, 11310–11323.

Chiche, D., Chaneac, C., Revel, R., and Jolivet, J. P. (**2011**). "Use of polyols as particle size and shape controllers: application to boehmite synthesis from sol-gel routes," Phys. Chem. Chem. Phys. **13**, 6241–6248.

Corma, A. and Fornes, V. (**1990**). "Cracking of N-Heptane on fluorinated gamma-alumina catalysts in the presence of hydrogen – catalytic activity and nature of acid active-sites," Appl. Catal. A-Gen. **61**, 175–185.

Dash, B., Tripathy, B. C., Bhattacharya, I. N., and Mishra, B. K. (**2010**). "Additive action on boehmite precipitation in sodium aluminate solution," Dalton Trans. **39**, 9108–9111.

Delgado-Pinar, E., Frias, J. C., Jimenez-Borreguero, L. J., Albelda, M. T., Alarcon, J., and Garcia-Espana, E. (**2007**). "One-pot preparation of surface modified boehmite nanoparticles with rare-earth cyclen complexes," Chem. Commun. **32**, 3392–3394.

Delgado-Pinar, E., Albelda, M. T., Frias, J. C., Barreiro, O., Tejera, E., Kubicek, V., Jimenez-Borreguero, L. J., Sanchez-Madrid, F., Toth, E., Alarcón, J., and Garcia-Espana, E. (**2011**). "Lanthanide complexes as imaging agents anchored on nano-sized particles of boehmite," Dalton Trans. **40**, 6451–6457.

Delgado-Pinar, E., Rotger, C., Costa, A., Pina, M. N., Jimenez, H. R., Alarcón, J., and Garcia-Espana, E. (**2012**). "Grafted squaramide monoamine nanoparticles as simple systems for sulfate recognition in pure water," Chem. Commun. **48**, 2609–2611.

Digne, M., Sautet, P., Raybaud, P., Toulhoat, H., and Artacho, E. (**2002**). "Structure and stability of aluminum hydroxides: a theoretical study," J. Phys. Chem. B **106**, 5155–5162.

Digne, M., Revel, R., Boualleg, M., Chiche, D., Rebours, B., Moreaud, M., Celse, B., Chaneac, C., and Jolivet, J. P. (**2010**). "Innovative characterizations and morphology control of gamma-AlOOH boehmite nanoparticles: towards advanced tuning of gamma-Al_2O_3 catalyst properties," Proceedings of the 10th International Symposium on Scientific Bases for the Preparation of Heterogeneous Catalysts **175**, 127–134.

Eberl, D. D., Srodon, J., Kralik, M., Taylor, B. E., and Peterman, Z. E. (**1990**). "Ostwald ripening of clays and metamorphic minerals," Science **248**, 474–477.

Edelman, R. (**1980**). "Vaccine adjuvants," Rev. Infect. Dis. **2**, 370–383.

Edelman, R. (**2001**). "The development and use of vaccine adjuvants," Mol. Biotechnol. **21**, 129–148.

Guzman-Castillo, M. L., Bokhimi, X., Toledo-Antonio, A., Salmones-Blasquez, J., and Hernandez-Beltran, F. (**2001**). "Effect of boehmite crystallite size and steaming on alumina properties," J. Phys. Chem. B **105**, 2099–2106.

He, T. B., Xiang, L., and Zhu, S. L. (**2009**). "Different nanostructures of boehmite fabricated by hydrothermal process: effects of pH and anions," Crystengcomm **11**, 1338–1342.

Iggland, M. and Mazzotti, M. (**2012**). "Population balance modeling with size-dependent solubility: ostwald ripening," Cryst. Growth Des. **12**, 1489–1500.

Jolivet, J. P., Froidefond, C., Pottier, A., Chaneac, C., Cassaignon, S., Tronc, E., and Euzen, P. (**2004**). "Size tailoring of oxide nanoparticles by precipitation in aqueous medium. A semi-quantitative modelling," J. Mater. Chem. **14**, 3281–3288.

Jolivet, J. P., Cassaignon, S., Chaneac, C., Chiche, D., and Tronc, E. (**2008**). "Design of oxide nanoparticles by aqueous chemistry," J. Sol-Gel Sci. Technol. **46**, 299–305.

Kaya, C., He, J. Y., Gu, X., and Butler, E. G. (**2002**). Nanostructured ceramic powders by hydrothermal synthesis and their applications," Microporous Mesoporous Mat. **54**, 37–49.

Kojdecki, M. A. (**2000**). "New criterion of regularisation parameter choice in Tikhonov's method," Biul. Mil. Univ. Technol. **XLIX**(1), 47–126.

Kojdecki, M. A., de Sola, E. R., Serrano, F. J., Delgado-Pinar, E., Reventós, M. M., Esteve, V. J., Amigó, J. M., and Alarcón, J. (**2007**). "Microstructural evolution of mullites produced from single-phase gels," J. Appl. Crystallogr. **40**, 260–276.

Kojdecki, M. A., de Sola, E. R., Serrano, F. J., Amigó, J. M., and Alarcón, J. (**2009**). "Comparative X-ray diffraction study of the crystalline microstructure of tetragonal and monoclinic vanadium-zirconium dioxide solid solutions produced from gel precursors," J. Appl. Crystallogr. **42**, 198–210.

Krokidis, X., Raybaud, P., Gobichon, A. E., Rebours, B., Euzen, P., and Toulhoat, H. (**2001**). "Theoretical study of the dehydration process of boehmite to gamma-alumina," J. Phys. Chem. B **105**, 5121–5130.

Langford, J. I. (**1978**). "Rapid method for analyzing breadths of diffraction and spectral-lines using voigt function," J. Appl.Crystallogr. **11**, 10–14.

Lock, N., Hald, P., Christensen, M., Birkedal, H., and Iversen, B. B. (**2010**). "Continuous flow supercritical water synthesis and crystallographic characterization of anisotropic boehmite nanoparticles," J. Appl. Crystallogr. **43**, 858–866.

Mathieu, Y., Lebeau, B., and Valtchev, V. (**2007**). "Control of the morphology and particle size of boehmite nanoparticles synthesized under hydrothermal conditions," Langmuir **23**, 9435–9442.

Moreaud, M., Jeulin, D., Morard, V., and Revel, R. (**2012**). "TEM image analysis and modelling: application to boehmite nanoparticles," J. Microsc. **245**, 186–199.

Nguefack, M., Popa, A. F., Rossignol, S., and Kappenstein, C. (**2003**). "Preparation of alumina through a sol-gel process. Synthesis, characterization, thermal evolution and model of intermediate boehmite," Phys. Chem. Chem. Phys. **5**, 4279–4289.

Okada, K., Nagashima, T., Kameshima, Y., Yasumori, A., and Tsukada, T. (**2002**). "Relationship between formation conditions, properties, and crystallite size of boehmite," J. Colloid Interface Sci. **253**, 308–314.

Pardo, P., Calatayud, J. M., and Alarcon, J. (**2014**). "Improvement of boehmite nanoparticles' aqueous dispersability by controlling their size, shape and crystallinity," RSC Adv. **4**, 48389–48398.

Pardo, P., Serrano, F. J., Vallcorba, O., Calatayud, J. M., Amigó, J. M., and Alarcón, J. (**2015**). "Enhanced lateral to basal surface ratio in boehmite nanoparticles achieved by hydrothermal aging," Cryst. Growth Des. **15**, 3532–3538.

Price, R. L., Gutwein, L. G., Kaledin, L., Tepper, F., and Webster, T. J. (**2003**). "Osteoblast function on nanophase alumina materials: influence of chemistry, phase, and topography," J. Biomed. Mater. Res. Part A **67A**, 1284–1293.

https://doi.org/10.1017/S0885715617000641 Published online by Cambridge University Press

Raybaud, P., Digne, M., Iftimie, R., Wellens, W., Euzen, P., and Toulhoat, H. (**2001**). "Morphology and surface properties of boehmite (gamma-AlOOH): a density functional theory study," J. Catal. **201**, 236–246.

Rutenberg, A., Vinogradov, V. V., and Avnir, D. (**2013**). "Synthesis and enhanced thermal stability of albumins@alumina: towards injectable sol-gel materials," Chem. Commun. **49**, 5636–5638.

Sanchez-Valente, J., Bokhimi, X., and Toledo, J. A. (**2004**). "Synthesis and catalytic properties of nanostructured aluminas obtained by sol-gel method," Appl. Catal. A-Gen. **264**, 175–181.

Santos, P. D., Coelho, A. C. V., Santos, H. D., and Kiyohara, P. K. (**2009**). "Hydrothermal synthesis of well-crystallised boehmite crystals of various shapes," Mater. Res.-Ibero-am. J. Mater. **12**, 437–445.

Scherrer, P. (**1918**). "Bestimmung der Grösse und der inneren Struktur von Kolloidteilchen mittels Röntgenstrahlen," Nachr. Ges. Wiss. Göttingen, **26 Juli**, 98–100.

Shen, S. C., Ng, W. K., Chia, L. S. O., Dong, Y. C., and Tan, R. B. H. (**2012**). "Morphology controllable synthesis of nanostructured boehmite and gamma-alumina by facile dry gel conversion," Cryst. Growth Des. **12**, 4987–4994.

Tettenhorst, R. and Hofmann, D. A. (**1980**). "Crystal-chemistry of boehmite," Clays Clay Min. **28**, 373–380.

Tikhonov, A. N., Goncharsky, A. V., Stepanov, V. V., and Yagola, A. G. (**1995**). *Numerical Methods for the Solution of Ill-posed Problems* (Kluwer, Dordrecht).

Webster, T. J., Hellenmeyer, E. L., and Price, R. L. (**2005**). "Increased osteoblast functions on theta plus delta nanofiber alumina," Biomaterials **26**, 953–960.

Wei, Y., Yang, R., Zhang, Y. X., Wang, L., Liu, J. H., and Huang, X. J. (**2011**). "High adsorptive gamma-AlOOH(boehmite)@SiO2/Fe3O4 porous magnetic microspheres for detection of toxic metal ions in drinking water," Chem. Commun. **47**, 11062–11064.

Xia, Y. G., Jiao, X. L., Liu, Y. J., Chen, D. R., Zhang, L., and Qin, Z. H. (**2013**). "Study of the formation mechanism of boehmite with different morphology upon surface hydroxyls and adsorption of chloride ions," J. Phys. Chem. C **117**, 15279–15286.

Yoldas, B. E. (**1973**). "Hydrolysis of aluminum alkoxides and bayerite conversion," J. Chem. Technol. Biotechnol. **23**, 803–809.

Zenobi, M. C., Luengo, C. V., Avena, M. J., and Rueda, E. H. (**2010**). "An ATR-FTIR study of different phosphonic acids adsorbed onto boehmite," Spectroc. Acta Pt. A-Molec. Biomolec. Spectr. **75**, 1283–1288.

Zhao, H. H., Song, H. L., Miao, Z. C., and Chou, L. J. (**2014**). "Isobutane dehydrogenation over chromia alumina catalysts prepared from MIL-101: insight into chromium species on activity and selectivity," J. Energy Chem. **23**, 708–716.

https://doi.org/10.1017/S0885715617000641 Published online by Cambridge University Press